sciendo

Research Article

Krzysztof Kurc*, Andrzej Burghardt, Dariusz Szybicki, and Józef Giergiel

Modeling the inspection robot with magnetic pressure pad

Abstract: This article presents the process of designing a robot with a magnetic pressure pad for inspections of ferromagnetic ventilation ducts. In compliance with the assumptions, the CAD design of the robot was developed in a 3D programming environment. The designing process brought about a mathematical model of the robot with one pair of magnetic drive modules, including simulation in a MATLAB/Simulink environment. The model accounted for parameters such as rolling resistance force, transverse resistance moment, magnetic attraction force, solid moment of inertia, and other factors. The magnetic pressure pad allowed for moving the robot in magnetic ventilation systems irrespective of slopes and shapes of ducts.

Keywords: Mechatronics, kinematics, dynamics, magnetic, inspection robot

1 Introduction

In terms of mechatronics, the inspection robotics is dedicated to the design of devices that may replace humans in the area of searching for information in dangerous and hard to access territories and sites. Particularly important and widespread developments in this branch of mechatronics are applied in military operations; exploration of dangerous and inaccessible environments, such as outer space; and, frequently, the inspection of pipelines containing liquid or gaseous utilities. The stated systems make up an environment that requires regular surveys in order to establish its condition. Given a difficult way in, access openings are often provided at the stage of construction.

The condition of ventilation systems is important to the extent requiring the implementation of special standards and directives to identify the admissible levels of impurities. Detailed analysis of dust composition and volume in a ventilation system calls for procedures of sampling and a visual survey. Thanks to the use of inspection robots, the entire process may be optimized. A mobile device may examine selected parameters by means of special measuring instruments. Expansion of the device by more modules allows conducting repairs or cleaning the systems.

Many other designs of mobile pipe inspection robots already exist, but majority of them possesses low level of adaptivity to the operating environment, mainly because of geometric limitations. In the article [1], authors focused on the design of wheeled inspection robots suitable for ϕ200-mm and ϕ85- to 109-mm round pipes that are based on a modular structure that features segments with wheeled legs on pantograph mechanisms for changes in diameter. Another concept was presented in article [2]. They designed four robot architectures using a rotor equipped with three pairs of tilted wheels moving on helical trajectories, propelling the robot forwards in the axial direction. The robots had different sizes for 170-, 70-, and 40-mm round pipes and allow only small changes in the diameter. In the article [3], authors proposed a platform with a cylindrical track drive, Omni-Track, that increases the contact area with pipes of different diameters and allow forward and backward motions along with side motion realized by a roll mechanism. A three-track vertical configuration for a constant pipe diameter was described.

Robots that can operate in ventilation ducts are mainly designed with focus on cleaning tasks. In the article [4], authors proposed a tracked platform with a guiding wheel intended for the operation with interchangeable brushes for horizontal ducts.

The market for inspection robots offers several solutions. Inuktun produces a wide range of tracked inspection robots. Versatrax models are available in three different sizes for minimal pipe diameters: 100, 150, and 300 mm [5]. Their main components are individually operated

***Corresponding Author: Krzysztof Kurc:** Rzeszow University of Technology, Faculty of Mechanical Engineering and Aeronautics; Email: kkurc@prz.edu.pl

Andrzej Burghardt: Rzeszow University of Technology, Faculty of Mechanical Engineering and Aeronautics; Email: andrzejb@prz.edu.pl

Dariusz Szybicki: Rzeszow University of Technology, Faculty of Mechanical Engineering and Aeronautics; Email: dszybicki@prz.edu.pl

Józef Giergiel: Institute of Technology, State University of Applied Sciences in Nowy Sącz; Email: jozef.giergiel@gmail.com

tracks of different sizes. Manually adjustable chassis allows adapting of the robot to sewer and storm drains, air ducts, tanks, oil and gas pipelines, and pulp and paper industries. Versatrax Vertical is a three-track version for a vertical, dry pipe inspection [6]. iPEK produces wheeled inspection vehicles, ROVVER, for pipes with a diameter of 100–300, 150–760, and 230–1520 mm [7]. These robots have modular designs with replaceable wheels, suitable for horizontal pipes and operation up to 10 m underwater. A Solo robot by RedZone is a tracked, wireless, autonomous robot that can be used in pipes with diameters ranging from 200 to 300 mm [8]. CUES offers tracked inspection robots for pipes with diameters that vary from 150 to 760 mm. Their main feature is a narrow track made of large segments [9]. As we may observe, numerous solutions for inspection robots are available. Wheels provide the least rolling resistance and are energy efficient; however, a small contact surface may not be sufficient for some uneven surfaces.

Among robots with magnetic modules, we should mention HISMAR that is described and designed for autonomic ship hull cleaning [10]. A number of advanced technologies allow mapping the hull, including details such as joints and crackings. The robot keeps to the ship's surface, thanks to its magnetic pressure pad. The pad includes 4 sets of electromagnets placed close to the robot wheels; the pads produce a magnetic field that is several times stronger than the field necessary to keep the robot in place. Magnebots, which is presented in [11] and [12], is a system for load transport under the ceiling. It contains a magnetic pad in the form of wheels with magnetic inserts. One wheel maintains up to 18 kg. This carrying power is achieved, thanks to suitable structure of the wheel, which is composed of ring-type neodymium magnets placed between steel plates and protected by rubber inserts.

The solution presented in this article covers the use of caterpillar-type magnetic modules and, in some way, is a novelty that will allow inspecting ferromagnetic ventilation systems and other systems in places inaccessible to other mobile units.

2 Drive system

The use of caterpillar-type modules composed of segments with neodymium magnets is one of the potential solutions to the problem of drive in robots with a magnetic pressure pad. By joining and closing the chain of such segments, we may obtain a caterpillar that should be set on the leading, driving, and adjusting wheels. Another solution to the

caterpillar drive problem is the use of a caterpillar made of a flexible belt. Magnetic pressure will be obtained by placing neodymium magnets in special pockets inside the (caterpillar) flexible belt. Drive will be first transferred onto the driving wheel and then onto the caterpillars by means of a transmission unit, which is shown in Figure 1.
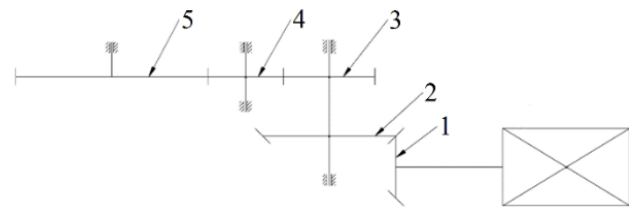

Figure 1: Kinematic diagram of drive system

Wheel 1 has been placed on the engine shaft; it cooperates with Wheel 2 that is placed on the shaft shared with Wheel 3. The latter transmits the torque through Wheel 4 onto Wheel 5 that is placed on the caterpillar driving wheel shaft. Total transmission of the gear unit is 8:1.

Figure 2 shows the entire unit, including the engine, placed inside the caterpillar module. Figure 3 shows the cross section of (caterpillar) flexible belt with neodymium magnets.
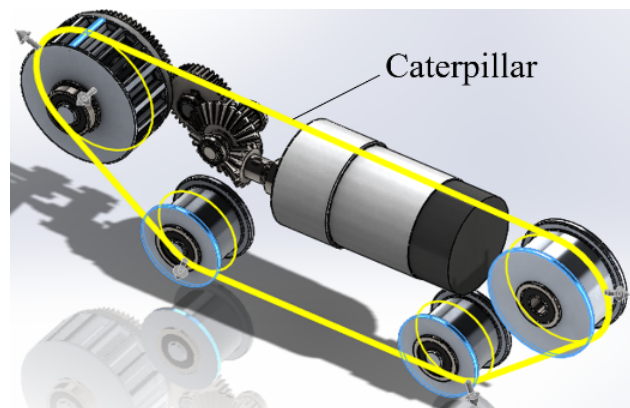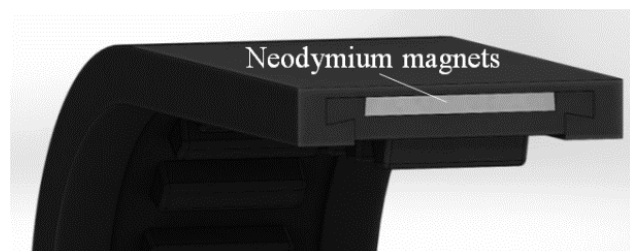

Figure 2: CAD model of drive unit

Figure 3: Cross section of caterpillar with neodymium magnets

The entire structure is closed in a box, ensuring the option to adapt the unit as a left-hand or right-hand drive module. Figure 4 shows a simplified CAD model of the robot showing caterpillar drives joined by the frame.
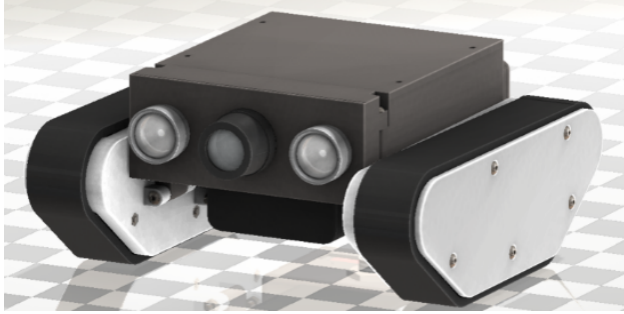

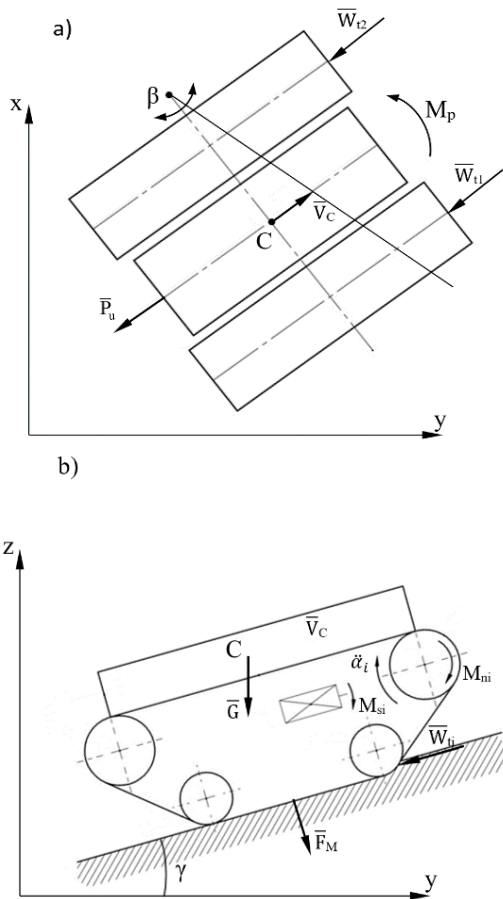**Figure 4:** Simplified CAD model of robot

Figure 5: Dynamic model of the robot—forces acting on the robot: (a) in the *xy* system and (b) in the *yz* system

3 Dynamics modeling

The dynamic description of the robot [13–24] was prepared using an energetic method based on the Lagrange equations. In order to avoid modeling problems with decoupling Lagrange multipliers, Maggi's equations were used [25]. In the dynamic model of the robot, the same characteristic points on the structure are considered as in the kinematic description (Figure 5a and 5b).

A description of dynamics was carried out by means of the second-order Lagrange equations for a nonholonomic system, which are given as follows [25]:

$$\frac{d}{dt}\left(\frac{\partial E}{\partial \dot{q}}\right)^T - \left(\frac{\partial E}{\partial q}\right)^T = Q + J^T(q)\lambda \qquad (1)$$

where $E = E(q, \dot{q})$ is the kinetic energy of the system, q is the configuration coordinate vector, Q is the configuration force vector, $J(q)$ is the Jacobian, and λ is the Lagrange multiplier vector.

Kinetic energy was determined as the sum of kinetic energies of individual elements of the robot:

$$E = E_R + E_{G1} + E_{G2} \qquad (2)$$

where E_R is the frame kinetic energy and E_{G1}, E_{G2} are the kinetic energy of the first and second caterpillar modules, respectively.

On the basis of the analysis, the kinetic energy equation of the robot (Eq. (2)) would adopt the following form:

$$E = \frac{1}{2}m_R\left(\dot{x}_C^2 + \dot{y}_C^2 + \dot{z}_C^2\right) + \frac{1}{2}I_R\dot{\beta}^2 \qquad (3)$$

$$+ \frac{1}{2}m\left(\left(\dot{x}_C - \frac{1}{2}H\dot{\beta}\sin\beta\right)^2 + \left(\dot{y}_C - \frac{1}{2}H\dot{\beta}\cos\beta\right)^2 + \dot{z}_C^2\right)$$

$$+ \frac{1}{2}m\left(\left(\dot{x}_C + \frac{1}{2}H\dot{\beta}\sin\beta\right)^2 + \left(\dot{y}_C + \frac{1}{2}H\dot{\beta}\cos\beta\right)^2 + \dot{z}_C^2\right)$$

$$+ \frac{1}{2}I_x\left(\dot{\alpha}_1^2 + \dot{\alpha}_2^2\right) + I_z\dot{\beta}^2$$

The left-side elements of the Lagrange equations were determined using Eq. (3).

To determine the right-side element of the Lagrange equations, the equations of kinematic constraints imposed on the system were defined:

$$\left.\begin{aligned}
\dot{x}_C - \frac{1}{2}r\dot{\alpha}_1(1-s_1)\sin\beta - \frac{1}{2}r\dot{\alpha}_2(1-s_2)\sin\beta &= 0 \\
\dot{y}_C - \frac{1}{2}r\dot{\alpha}_1(1-s_1)\cos\beta\cos\gamma \\
-\frac{1}{2}r\dot{\alpha}_2(1-s_2)\cos\beta\cos\gamma &= 0 \\
\dot{z}_C - \frac{1}{2}r\dot{\alpha}_1(1-s_1)\sin\gamma - \frac{1}{2}r\dot{\alpha}_2(1-s_2)\sin\gamma &= 0
\end{aligned}\right\} \qquad (4)$$

The nonholonomic constraint equations may be expressed as follows:

$$J(q)\,\dot{q} = 0 \qquad (5)$$

Then the Jacobian is expressed as follows:

$$J(q) = \qquad (6)$$

$$\begin{bmatrix} 1 & 0 & 0 & 0 & -\frac{1}{2}r(1-s_1)\sin\beta & -\frac{1}{2}r(1-s_2)\sin\beta \\ 0 & 1 & 0 & 0 & -\frac{1}{2}r(1-s_1)\cos\beta\cos\gamma & -\frac{1}{2}r(1-s_2)\cos\beta\cos\gamma \\ 0 & 0 & 1 & 0 & -\frac{1}{2}r(1-s_1)\sin\gamma & -\frac{1}{2}r(1-s_2)\sin\gamma \end{bmatrix}$$

and the vector $\dot{q}$ is expressed as follows:

$$\dot{q} = \begin{bmatrix} \dot{x}_C & \dot{y}_C & \dot{z}_C & \dot{\beta} & \dot{\alpha}_1 & \dot{\alpha}_2 \end{bmatrix}^T \qquad (7)$$

Then, the vector Q will become

$$Q = \qquad (8)$$

$$\begin{bmatrix} 0 \\ 0 \\ 0 \\ -M_p \\ M_{n1} + \left(-\frac{1}{2}P_u - \frac{1}{2}G\sin\gamma - \frac{1}{2}F_M - W_{t1} \right) r(1-s_1) \\ M_{n2} + \left(-\frac{1}{2}P_u - \frac{1}{2}G\sin\gamma - \frac{1}{2}F_M - W_{t2} \right) r(1-s_2) \end{bmatrix}$$

After the transformation, we received six unknown coordinates and three unknown Lagrange's multipliers, which made the system of equations intractable. Hence, we applied Maggie's formalism [25–27]:

$$C(q)\left(\frac{d}{dt}\left(\frac{\partial E}{\partial \dot{q}} \right) - \left(\frac{\partial E}{\partial q} \right) \right) = C(q)\,Q \qquad (9)$$

Matrix C form was derived:

$$C^T(q) = \qquad (10)$$

$$\begin{bmatrix} \frac{1}{2}r(1-s_1)\sin\beta & \frac{1}{2}r(1-s_2)\sin\beta \\ \frac{1}{2}r(1-s_1)\cos\beta\cos\gamma & \frac{1}{2}r(1-s_2)\cos\beta\cos\gamma \\ \frac{1}{2}r(1-s_1)\sin\gamma & \frac{1}{2}r(1-s_2)\sin\gamma \\ -\frac{r(1-s_1)}{H} & \frac{r(1-s_2)}{H} \\ 1 & 0 \\ 0 & 1 \end{bmatrix}$$

Next, we solved the right-side element of Maggie's equation:

$$C(q)\,Q = \qquad (11)$$

$$\begin{bmatrix} M_{n1} + \left(-\frac{1}{2}P_u - \frac{1}{2}G\sin\gamma - \frac{1}{2}F_M - W_{t1} \right)(1-s_1)r + \frac{M_p r(1-s_1)}{H} \\ M_{n2} + \left(-\frac{1}{2}P_u - \frac{1}{2}G\sin\gamma - \frac{1}{2}F_M - W_{t2} \right)(1-s_2)r - \frac{M_p r(1-s_2)}{H} \end{bmatrix}$$

The above analysis allows for expressing Maggie's equations and then the relationships that are solutions to the inverse and simple problem of robot dynamics. In order to analyze such problems, we need to define the towing force, P_u; magnetic interaction force, F_M; caterpillar rolling resistance force, W_t; and transverse resistance moment, M_p.

3.1 Towing force

In this case, the wiring towed by the robot will have the only impact on the towing force. We dropped the impact of resistances connected with wiring unwinding. To simplify the analysis, we assumed that the towing force would be equal to the wiring load:

$$P_U = \rho_K gs \qquad (12)$$

where ρ_K is the mass of one running meter of wiring, g is the gravitational acceleration, and s is the distance covered.

3.2 Magnetic interaction force

The magnetic pressure system contains rectangular magnets placed inside the flexible caterpillar. The force of attraction of one rectangular magnet [28] whose dimensions are $a \times b \times c$, which is placed at a certain distance from the steel plate (Figure 6), amounts to

$$F_M = \frac{AB_X^2}{\mu} \qquad (13)$$

where A is the area of the plane adjacent (parallel) to the attracted object, $\mu = 4\pi\,10^{-7}$ H/m is the magnetic permeability of vacuum, and B_X(T) is the magnetic induction.
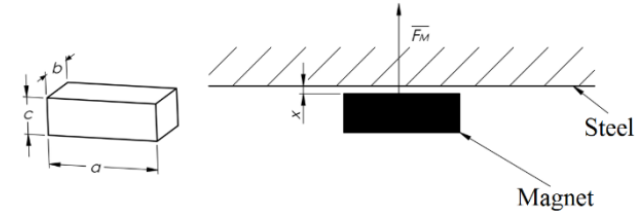

Figure 6: Magnetic attraction force

The value of magnetic induction [28] can be calculated using the following equation:

$$B_X = \frac{B_r}{\pi} \left(\begin{array}{l} a\tan\frac{ab}{2x\sqrt{4x^2+a^2+b^2}} - \\ a\tan\frac{ab}{2(c+x)\sqrt{4(c+x)^2+a^2+b^2}} \end{array} \right) \qquad (14)$$

where B_r is the remanence, a distinguishing feature of magnet material.

In this design, a single magnet has the following dimensions: $a = 20$ mm, $b = 4$ mm, $c = 1.8$ mm, $x = 1.2$ mm, and $B_r = 1.4$ T—for material N42 according to [28].

For the above data, including the fact that in a single caterpillar drive, the number of magnets that contact the

ground is equal to 17 and the force generated by a single magnet amounts to 8.35 N, we have checked the impact of distance on the force F_M. The distance is not constant and may change because of the impact of, for example, layer of dust deposits inside a duct. Assuming that the fluctuations are contained within the limits $x \in < 1, 2; 2, 7 >$, Figure 7 was obtained.
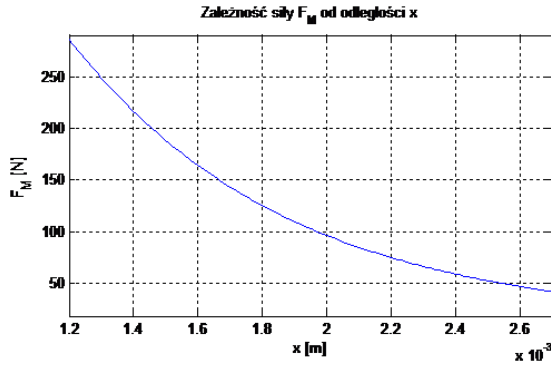

Figure 7: Attraction force in the function of distance

At the minimum possible distance, the attraction force exceeds 286 N; it decreases, however, along with the increase in the distance and achieves the value of 41.9 N at the maximum assumed distance of 2.7 mm. On the other hand, we must mention here that the dust will be compressed while the vehicle is moving.

3.3 Rolling resistance force

The rolling resistance force is the result of interactions with the ground; it is produced through pushing aside and compressing the ground.

$$W_t = (G \cos \gamma + F_M) f_g \tag{15}$$

Rolling resistance coefficient, f_g, depends on the mechanical parameters of the robot and the ground. It is determined through experimentation; for instance, for a dry sandy road, it amounts to $f_g = 0.07$ [15].

3.4 Transverse resistance moment

The transverse resistance moment appears only when the track-laying vehicle takes a turn. It results from the interactions of transverse forces while the caterpillar modules are turning. In a simplified model that does not account for nonuniformal distribution of pressures between the caterpillar and the ground, the aforesaid moment takes the

form of the towing force, assuming that the rotation occurs at a constant velocity [29]:

$$M_p = 2 \int_0^{0,5L} \mu_p \frac{G \cos \gamma + F_M}{L} x dx \tag{16}$$
$$= \frac{\mu_p (G \cos \gamma + F_M) L}{4}$$

where μ_p is the transverse resistance moment depending on the caterpillar structure, ground parameters, and robot motion parameters. The maximum value of transverse resistance moment is

$$\mu_{p \max} = (0.7 \div 0.75) \mu \tag{17}$$

where μ is the caterpillar tractive adherence coefficient; for a dry sandy road, its value is assumed as $\mu = 0.7$ [15].

The relationship between the transverse resistance moment and the turning radius is expressed as follows:

$$\mu_p = \frac{\mu_{p \max}}{3.5 + \frac{R}{b}} \tag{18}$$

where R is the turning radius and b is the width of the caterpillar.

Finally, the transverse resistance moment equation is expressed as follows:

$$M_p = \frac{0.75 \mu (G \cos \gamma + F_M) L}{14 + \frac{4 V_c}{\dot{\beta} b}} \tag{19}$$

4 Digital experiment

The mathematical analysis was followed by the simulation of the kinematic inverse problem in a MATLAB/Simulink environment. We assumed that the point C motion path of the robot would include the following 9 stages (Figure 8):
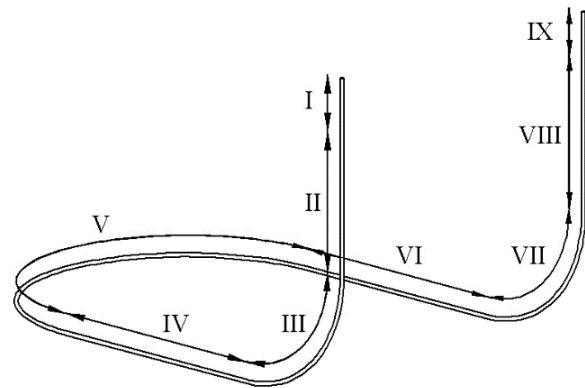

Figure 8: Individual stages of robot point C motion path

Stage I: driving down a vertical surface, start-up:

$$V_C = \frac{V_X}{t_r}(t - t_p), \ t_p \le t \le t_r, \ \dot{\alpha}_1 = \dot{\alpha}_2 = \frac{V_C}{r}, \dot{\beta} = 0,$$
$$\gamma = -\frac{\pi}{2},$$

where V_X is the maximum velocity and t_p, t_r are the time of beginning and ending of the motion, respectively.

Stage II: driving down the vertical surface at a steady velocity:

$$V_C = V_X, \ t_p \le t \le t_r, \ \dot{\alpha}_1 = \dot{\alpha}_2 = \frac{V_C}{r}, \dot{\beta} = 0, \ \gamma = -\frac{\pi}{2}.$$

Stage III: entering the horizontal plane from the vertical plane:

$$V_C = V_X, \ t_p \le t \le t_r, \ \dot{\alpha}_1 = \dot{\alpha}_2 = \frac{V_C}{r}, \dot{\beta} = 0,$$
$$\gamma = -\frac{\pi}{2}\left(\frac{t_r - t}{t_p}\right).$$

Stage IV: driving on the horizontal plane at a steady velocity:

$$V_C = V_X, \ t_p \le t \le t_r, \ \dot{\alpha}_1 = \dot{\alpha}_2 = \frac{V_C}{r}, \dot{\beta} = 0, \ \gamma = 0.$$

Stage V: driving along a circle with a radius R, including the transient period of entering the circular arc:

$$V_C = V_X, \ t_p \le t \le t_r, \ \dot{\alpha}_1 = \frac{V_C}{r} - H\dot{\beta}, \ \dot{\alpha}_2 = \frac{V_C}{r} + H\dot{\beta},$$
$$\dot{\beta} = \frac{V_C}{R}, \ \gamma = 0.$$

Stage VI: driving on the horizontal surface at a steady velocity:

$$V_C = V_X, \ t_p \le t \le t_r, \ \dot{\alpha}_1 = \dot{\alpha}_2 = \frac{V_C}{r}, \ \dot{\beta} = 0, \ \gamma = 0.$$

Stage VII: entering the vertical surface:

$$V_C = V_X, \ t_p \le t \le t_r, \ \dot{\alpha}_1 = \dot{\alpha}_2 = \frac{V_C}{r}, \ \dot{\beta} = 0,$$
$$\gamma = \frac{\pi}{2}\left(\frac{t - t_p}{t_p}\right).$$

Stage VIII: driving up the vertical surface at a steady velocity:

$$V_C = V_X, \ t_p \le t \le t_r, \ \dot{\alpha}_1 = \dot{\alpha}_2 = \frac{V_C}{r}, \ \dot{\beta} = 0, \ \gamma = \frac{\pi}{2}.$$

Stage IX: braking:

$$V_C = V_X - \frac{V_X}{t_r - t_p}(t - t_p), \ t_p \le t \le t_r, \ \dot{\alpha}_1 = \dot{\alpha}_2 = \frac{V_C}{r},$$
$$\dot{\beta} = 0, \ \gamma = \frac{\pi}{2}.$$

The point C linear velocity relationship was used in order to smooth the start-up and braking operations:

$$V_c = V_x \left(\frac{1}{1 + e^{(-c(t-b_1))}} - \frac{1}{1 + e^{(-c(t-b_2))}}\right) \tag{20}$$

where c is the robot acceleration and braking coefficient and b_1, b_2 are the time of beginning the acceleration and braking, respectively.

The fluctuation of the value of ascending vertical angle, γ, was modeled so as to make the vehicle to begin its motion on the vertical surface and then todrive down and enter the horizontal surface (Figure 8). After such maneuvers, the vehicle would enter the vertical surface:

$$\gamma = -\frac{\pi}{2}\left(\frac{1}{1 + e^{(-c_g(t-b_{g1}))}} - \frac{1}{1 + e^{(-c_g(t-b_{g2}))}}\right) \tag{21}$$
$$+ \frac{\pi}{2}\left(\frac{1}{1 + e^{(-c_g(t-b_{g3}))}} - \frac{1}{1 + e^{(-c_g(t-b_{g4}))}}\right)$$

where c_g is the coefficient representing the turning radius; b_{g1}, b_{g2} are the time of beginning and ending the drive down the vertical surface, respectively; and b_{g3}, b_{g4} are the time of beginning and ending the drive up the vertical surface, respectively.

Angular velocities of the driving wheel were described by means of the following relationships:

$$\dot{\alpha}_1 = \frac{V_c}{r(1 - s_1)} \tag{22}$$
$$- \frac{H}{2r(1 - s_1)}\dot{\beta}\left(\frac{1}{1 + e^{(-c_a(t-b_{a1}))}} - \frac{1}{1 + e^{(-c_a(t-b_{a2}))}}\right)$$

$$\dot{\alpha}_2 = \frac{V_c}{r(1 - s_2)} \tag{23}$$
$$+ \frac{H}{2r(1 - s_2)}\dot{\beta}\left(\frac{1}{1 + e^{(-c_a(t-b_{a1}))}} - \frac{1}{1 + e^{(-c_a(t-b_{a2}))}}\right)$$

where c_a is the coefficient of velocity of entering and leaving the circular arc; b_{a1}, b_{a2} are the time of entering and leaving the circular arc, respectively; and s_1, s_2 are the caterpillar skid, respectively.

The following are the simulation data:
V_x = 0.1m/s, H = 202mm, r = 22.7mm, s_1 = s_2 = 0, R = 0.4m, c = 5, b_1 = 2s, b_2 = 28s, c_a = 5, b_{a1} = 10s, b_{a2} = $b_{a1} + \frac{R\pi}{V_x}$, c_g = 2, b_{g1} = −5s, b_{g2} = 5s, b_{g3} = 27.5s, b_{g4} = 40s, m_R = 2kg, m = 1kg, ρ_k = 0.2kg/m, b = 34mm, L = 100mm, I_R = 0.0021kg/m^2, I_Z = 0.008kg/m^2, I_x = 0.00006kg/m^2.

Masses and solid moments of inertia were found based on the parameters from the CAD software module.

The following is the point C motion path (Figure 9) according to the assumptions: the robot begins to move on the vertical surface of the ventilation duct; next, it drives

down to enter the horizontal surface where it executes the turning maneuver to approach the vertical surface and enter that surface.

The robot velocity pattern (Figure 10) has three individual stages: accelerating, driving at a steady velocity, and braking.

The first value of the ascending vertical angle, γ (Figure 11), is $-\frac{\pi}{2}$, which corresponds to the downward position of the robot on a vertical wall. The angle assumes the value of 0 when the robot drives on the horizontal surface; afterwards, it increases up to $\frac{\pi}{2}$, which corresponds to the robot driving in its vertical position.

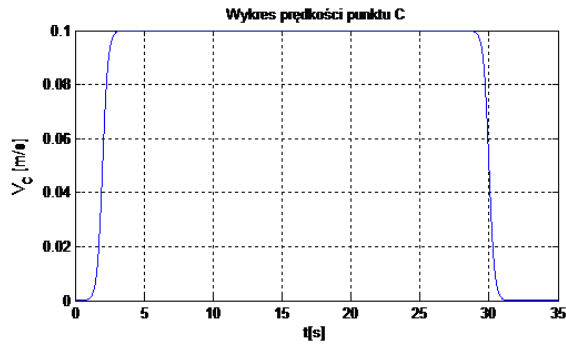Robot frame rotation angle, β (Figure 12), increases to achieve the value of π, that is, half circle, during the turn. Its uniform increase is a signal that the robot moves along a circle of radius R.

The pattern of robot frame angular velocity, $\dot{\beta}$ (Figure 13), represents the way and the time of variation of the analyzed quantity. When the robot executes a maneuver, the velocity, $\dot{\beta}$, achieves its maximum value. The velocity with a value of 0 occurs when the robot drives along a straight line, irrespective of the ascending vertical angle.

Figures 14–16 show the changes in kinematic parameters of driving wheel rotary motion.
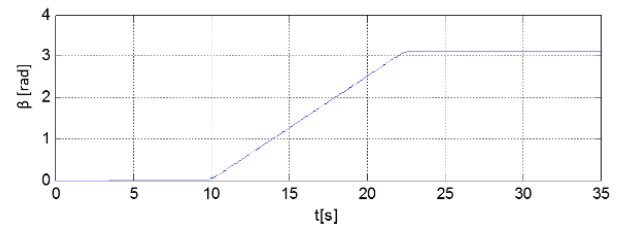

Figure 9: Point C motion path

Figure 10: Point C velocities
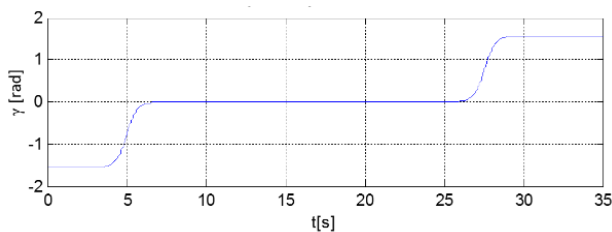
Figure 11: Ascending vertical angle

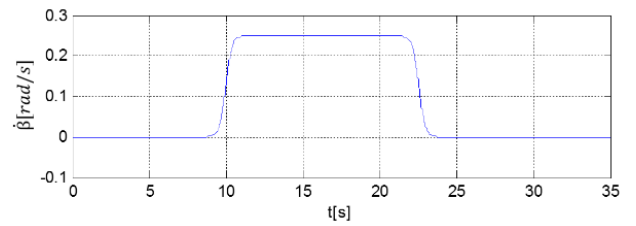**Figure 12:** Rotation angle of the robot frame

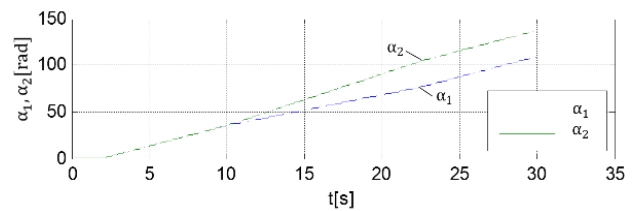**Figure 13:** Angular velocity of the robot frame

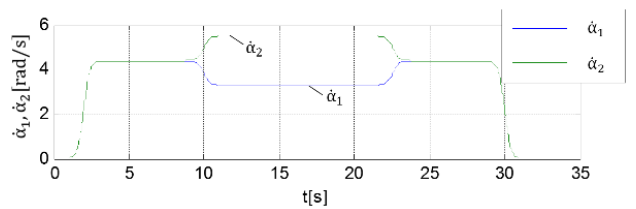**Figure 14:** Rotation angles of the caterpillar driving wheel

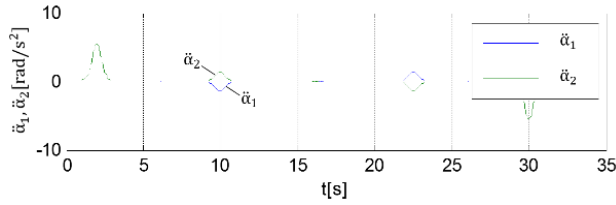
Figure 15: Angular velocities of the caterpillar driving wheel

Figure 16: Angular acceleration of the caterpillar driving wheel

Figure 17: Diagram of caterpillar driving wheel moments

The patterns of rotation angle (Figure 14) are parallel when the robot drives along a straight line. Change will occur if the robot enters the turn; at the end of the turning maneuver, the patterns will become parallel again.

When the vehicle turns, the angular velocities of the driving wheel (Figure 15) adopt different values, which is a condition precedent to the turning maneuver. Out of the turn, the velocities will feature the same pattern.

The values of angular acceleration (Figure 16) are other than zero in the period of acceleration and braking as well as during the turning maneuvers.

The pattern of driving moments (Figure 17) allows for concluding that the driving moment value will be 0 if the robot comes to a standstill. The maximum value that caterpillar driving wheel moments achieve is 2.73 Nm. Assuming the gear ratio as $i = 8$ and efficiency as $\eta = 0.8$, the maximum values of moments on engine shafts will be

$$M_S = \frac{M_n}{i\eta} = 0.41 \text{Nm} \qquad (24)$$

The engine must achieve the rotations mentioned as follows:

$$n_S = i\alpha_{\max}\frac{60}{2\pi} \qquad (25)$$

where $\alpha_{\max}$ is the maximum angular velocity of the driving wheel resulting from the kinematic inverse problem and amounting to $\alpha_{\max} = 5.51$ rad/s. We receive the value $n_S = 420$ obr/min. On this basis, we selected the DC current engine 37Dx68L manufactured by Pololu, containing the integrated 19:1 transmission unit. The engine turning moment amounts to $M_S = 0.5$ Nm, whereas the rotations (rpm) are $n_S = 500$ obr/min.

5 Conclusions

The installation of the magnetic pressure pad extends the potential to move inside the ventilation systems, irrespective of slopes and shapes of the ducts. A ventilation duct was selected as the working environment of the robot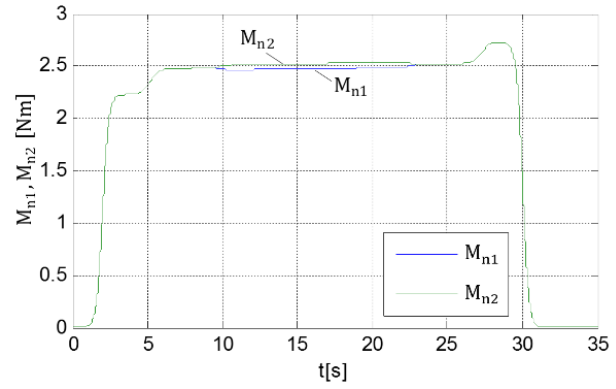; the drive developed by the authors, however, may be easily used in other systems, such as pipelines, water supply, or drainage systems.

The design of the robot allows for the inspection of ventilation ducts featuring various configurations. Thanks to the adaptation of the robot to a smooth transition from vertical to horizontal walls, the unit is able to survey a considerable part of the system with no need to reconfigure its arrangement.

The design was built so as to ensure the option of expansion. The design of the magnetic pressure pad was developed in the form of the caterpillar module that may be successfully applied as a module for driving another robot.

A problem in the area of pipeline inspection is the fact that pipelines happen to take complex shapes, which requires the designers to build units capable of moving in both vertical and horizontal directions. If the robot is equipped with the magnetic pressure pad, which allows it to remain on the surface irrespective of the angle of inclination, such a solution will successfully eliminate the aforesaid problem. A magnetic pressure pad, however, has considerable limitations because the robot will be able to use its functions entirely only in the case of the systems built of ferromagnetic materials.

References

[1] Choi H.R., Roh S.: In-pipe robot with active steering capability for moving inside of pipelines. [In:] Bioinspiration and Robotics Walking and Climbing Robots, InTech, 375-402, 2007.

[2] Horodinca M.H., Doroftei I., Mignon E., Preumont A.: A simple architecture for in-pipe inspection robots.Proceedings of International Colloquium on Mobile and Autonomous Systems, 61-64, 2002.

[3] Tadakuma K., Ming A., Shimojo M., Tadakuma R., NagataniK., Yoshida K., Iagnemma K.: Basic running test of the cylindrical tracked vehicle with sideways mobility. InIntelligent Robots and

Systems, IROS 2009. IEEE/RSJ International Conference on,1679-1684, 2009.

[4] Wang Y., & Zhang J.: Autonomous air duct cleaning robot system. InCircuits and Systems,MWSCAS'06. 49th IEEE International Midwest Symposium on,1, 510-513, 2006.

[5] Inuktun: Inuktun crawler vehicles, http://www.inuktun.com/crawler-vehicles, accessed on 24.04.2012.

[6] Hydropulsion: Vertical Crawler Specification Sheet, http://www.hydropulsion.com/roboticcrawler-systems/vertical-crawler/verticalcrawler.pdf, accessed on 24.04.2012.

[7] Ipek: ROVVER Brochure, http://www.ipek.at/fileadmin/FILES/downloads/brochures/iPEKrovverweben.pdf, accessed on 08.03.2012.

[8] Redzone: SOLO Unmanned Inspection Robot, http://www.redzone.com/products/solo%C2%AE, accessed on 24.04.2012.

[9] Cues: Ultra Shorty III, http://www.cuesinc.com/UltraShortyIII.html, accessed on 24.04.2012.

[10] Narewski M.: HISMAR-underwater hull inspection and cleaning system as a tool for ship propulsion system performance increase.Journal of Polish CIMAC,4(2), 227-234, 2009.

[11] Slocum A. H., Awtar S., & Hart J.:Magnebots–a magnetic wheels based overhead transportation concept.IFAC Proceedings Volumes, 35(2), 761-766, 2002.

[12] Slocum A., Lang J., Awtar S., Hart A. J., & Mukaddam K.: Magnetically preloaded wheels. InProc. 4th Inter. Conf. of the European Society of Precision Engineering and Nanotechnology,2004.

[13] Burdziński Z.: Theory of Motion of a Tracked Vehicle (in Polish).Wydawnictwa Komunikacji i Łączności, Warszawa,1972.

[14] Chodkowski A.W.: Design and Calculations of High Speed Tracked Vehicles (in Polish). Wydawnictwa Komunikacji i Łączności, Warszawa,1990.

[15] Dajniak H.: Tractors, Theory of Motion and Design (in Polish). Wydawnictwa Komunikacji i Łączności, Warszawa,1985.

[16] Żylski W.: Kinematics and Dynamics of Wheeled Mobile Robots (in Polish).Oficyna Wydawnicza Politechniki Rzeszowskiej, Rzeszow,1996.

[17] Giergiel J.,Kurc K.: Identification of the mathematical model of an inspection mobile robot with fuzzy logic systems and neural networks.Journal of Theoretical and Applied Mechanics,vol. 49(1), 209-225, 2011.

[18] Kurc K., Szybicki D.: Kinematics of a Robot with Crawler Drive. Mechanics and Mechanical Engineering, 15(4), 93-101, 2011.

[19] Giergiel J., Kurc K.: Modelling and identification of the superintending mobile robot. Mechanics and Mechanical Engineering, 13(2), 23-31, 2009.

[20] Gierlak P., Kurc K.,Szybicki D.: Mobile crawler robot vibration analysis in the contexts of motion speed selection.Journal of Vibroengineering,19(4),2403-2412,2017.

[21] Tutak J. S.: Design of ELISE robot for the paretic upper limb of stroke survivors. Journal of Vibroengineering,18(6), 4069-4085,2016.

[22] Tutak J. S., Wiech J.: Horizontal automated storage and retrieval system. Advances in Science and Technology Research Journal,11(1), 82-95, 2017.

[23] Giergiel M., Buratowski T., Małka P., Kurc K., Kohut P., Majkut K.: The project of tank inspection robot. Key Engineering Materials, Trans Tech Publications,518, 375-383, 2012.

[24] Ciszewski M., Buratowski T., Giergiel M., Kurc K., Małka P.: Mobile inspection robot. Applied Mechanics and Materials, 319, 385-392, 2013.

[25] Giergiel J., Żylski W.: Description of motion of a mobile robot by Maggie's equations. Journal of Theoretical and Applied Mechanics,43(3), 511-521, 2005.

[26] Ciszewski M., Wacławski M., Buratowski T., Giergiel M., Kurc K.: Design, modelling and laboratory testing of a pipe inspection robot. Archive of Mechanical Engineering,62(3), 395-408,2015.

[27] Kurc K., Szybicki D., Burghardt A., Muszyńska M.: The application of virtual prototyping methods to determine the dynamic parameters of mobile robot. Open Engineering,6(1), 55-63, 2016.

[28] Magnetismus:http://www.ibsmagnet.de/pdf/de/ibs_d.pdf, 2013.

[29] Giergiel J., Kurc K., Szybicki D.: Mechatronics of the inspection robots with crawler drive (in Polish), ISBN 978-83-7199-963-1, Oficyna Wydawnicza Politechniki Rzeszowskiej, Rzeszow.2014.